

PAPER

## Dendron based antifouling, MRI and magnetic hyperthermia properties of different shaped iron oxide nanoparticles

To cite this article: G Cotin *et al* 2019 *Nanotechnology* **30** 374002

View the [article online](#) for updates and enhancements.








**IOP | ebooks™**

Bringing you innovative digital publishing with leading voices to create your essential collection of books in STEM research.

Start exploring the **collection** - **download the first chapter of every title for free.**

# Dendron based antifouling, MRI and magnetic hyperthermia properties of different shaped iron oxide nanoparticles

G Cotin<sup>1,2</sup>, C Blanco-Andujar<sup>1,2</sup>, D-V Nguyen<sup>1,2</sup>, C Affolter<sup>3</sup>, S Boutry<sup>4,5</sup>,  
A Boos<sup>6,7</sup> , P Ronot<sup>6,7</sup>, B Uring-Lambert<sup>8</sup>, P Choquet<sup>9,10,11,12</sup>, P E Zorn<sup>13,14</sup>,  
D Mertz<sup>1,2</sup> , S Laurent<sup>4,5</sup> , R N Muller<sup>4,5</sup>, F Meyer<sup>3</sup> ,  
D Felder Flesch<sup>1,2</sup> and S Begin-Colin<sup>1,2,15</sup> 

<sup>1</sup> Université de Strasbourg, CNRS, Institut de Physique et Chimie des Matériaux de Strasbourg, UMR 7504, F-67034 Strasbourg, France

<sup>2</sup> Labex CSC, Fondation IcFRC/université de Strasbourg, 8 allée Gaspard Monge BP 70028, F-67083 Strasbourg Cedex, France

<sup>3</sup> Université de Strasbourg, INSERM, UMR 1121 Biomaterials and Bioengineering, FMTS, F-67000 Strasbourg, France

<sup>4</sup> University of Mons, General, Organic and Biomedical Chemistry, NMR and Molecular Imaging Lab, Avenue Maistriau 19, B-7000 Mons, Belgium

<sup>5</sup> CMMI, Center for Microscopy and Molecular Imaging, Rue Adrienne Bolland 8, B-6041 Gosselies, Belgium

<sup>6</sup> University of Strasbourg, IPHC, 25 rue Becquerel F-67087 Strasbourg, France

<sup>7</sup> CNRS, UMR7178, F-67087 Strasbourg, France

<sup>8</sup> Laboratoire Central d'Immunologie, Fédération Hospitalo-Universitaire OMICARE, Fédération de Médecine Translationnelle de Strasbourg, Nouvel Hôpital Civil, F-67091 Strasbourg Cedex, France

<sup>9</sup> Imagerie Préclinique—UF6237, Pôle d'imagerie, Hôpitaux Universitaires de Strasbourg, France

<sup>10</sup> Icube, équipe MMB, CNRS, Université de Strasbourg, Strasbourg, France

<sup>11</sup> Fédération de Médecine Translationnelle de Strasbourg, Faculté de Médecine, Université de Strasbourg, Strasbourg, France

<sup>12</sup> AMT Lab, Dept. of Biomedical Engineering, University of Basel, Allschwil, Switzerland

<sup>13</sup> Imagerie Préclinique—UF6237, Pôle d'imagerie, Hôpitaux Universitaires de Strasbourg, France

<sup>14</sup> Service de Radiologie 2, Haute-pierre, Pôle d'imagerie, Hôpitaux Universitaires de Strasbourg, France

E-mail: [Sylvie.begin@ipcms.unistra.fr](mailto:Sylvie.begin@ipcms.unistra.fr)

Received 19 November 2018, revised 10 May 2019

Accepted for publication 13 June 2019

Published 3 July 2019



## Abstract

Owing to the great potential of iron oxide nanoparticles (NPs) for nanomedicine, large efforts have been made to better control their magnetic properties, especially their magnetic anisotropy to provide NPs able to combine imaging by MRI and therapy by magnetic hyperthermia. In that context, the design of anisotropic NPs appears as a very promising and efficient strategy. Furthermore, their bioactive coating also remains a challenge as it should provide colloidal stability, biocompatibility, furtivity along with good water diffusion for MRI. By taking advantage of our controlled synthesis method of iron oxide NPs with different shapes (cubic, spherical, octopod and nanoplate), we demonstrate here that the dendron coating, shown previously to be very suitable for 10 nm sized iron oxide, also provided very good colloidal, MRI and antifouling properties to the anisotropic shaped NPs. These antifouling properties, demonstrated through several experiments and characterizations, are very promising to achieve specific targeting of disease tissues without affecting healthy organs. On the other hand, the magnetic hyperthermia properties were shown to depend on the

<sup>15</sup> Author to whom any correspondence should be addressed.

saturation magnetization and the ability of NPs to self-align, confirming the need of a balance between crystalline and dipolar magnetic anisotropies.

Supplementary material for this article is available [online](#)

Keywords: iron oxide nanoparticles, nanocubes, octopods, nanoplates, dendron coating, MRI, magnetic hyperthermia

(Some figures may appear in colour only in the online journal)

## 1. Introduction

Despite the progress achieved in cancer treatment during the last decades, new approaches are needed to improve the existing therapies or developing new technologies that reduce the deleterious side-effects and increase patient survival rates. To face this challenge, research in the synthesis and functionalization of inorganic nanoparticles (NPs) has aimed at developing multifunctional theranostic NPs. These systems combine both therapeutic and multimodal imaging components, which allow to follow the effect of the therapy by imaging and can also act locally in tumours to avoid side-effects [1–9].

In that context, iron oxide NPs have been the system of choice due to their interesting magnetic properties, low toxicity and biocompatibility. They have been used for diagnosis as contrast agent (CA) in magnetic resonance imaging (MRI) (already commercialized as  $T_2$  CA for MRI) and for therapy in magnetic hyperthermia (MH), making them potential theranostic nanoplateforms. Yet, in order to be efficient for both applications, iron oxide NPs need to be specially designed [10] and coated with suitable molecules.

Indeed for biomedical applications, a key point in theranostic nanoparticle development is the design of the organic coating [11, 12]. The molecules anchored at the surface of the NPs can provide different functions, such as dyes for optical imaging, targeting ligands to reach target tissue or cells, or therapeutic agents (drug delivery). At the same time, the organic coating must prevent NPs from agglomeration in a physiological environment and enhance their biodistribution and bioelimination. Besides polymers which have been widely studied up to now, another class of molecule is emerging i.e. small dendrons [13–16]. Bifunctional dendrons are a promising option as the diversity of functionalization brought by the arborescent structure simultaneously solves the need for biocompatibility, low toxicity, *in vivo* stability and specificity. The grafting of dendrons on the surface of 10 nm iron oxide NPs using a phosphonate group as coupling agent has led to a new generation of MRI CAs [17–19]. These nano-objects display relaxivity values higher than those of commercial CAs and also provide good biodistribution in mice without a significant uptake in healthy tissues (good bioelimination) [20–23]. The use of such dendrons appears as a good way to ensure, after the grafting step, a mean particle size below 100 nm together with a narrow size distribution in suspension, both being prerequisites for a good biodistribution, i.e. avoiding RES uptake. Recent *in vitro* and *in vivo* results with 10 nm sized spherical NPs confirmed that they do not internalize in cells and accumulate in organs after IV injection [17, 18, 24].

Concerning the magnetic core, most current published iron oxide NPs (IONPs) display suitable properties as CAs for MRI as the main requirements are: good saturation magnetization, a coating ensuring a suitable water diffusion and a limited aggregation state [24]. Significant effort is now focused on their design optimization to provide more efficient agents for magnetic hyperthermia (MH). When magnetic NPs are exposed to alternating magnetic fields, heat may be locally released (where they are concentrated), leading to a reduction in cell viability in cancer cells. The potential of MH was demonstrated with the favourable results of the ‘nanothermotherapy’ study in clinical phase II led by the German company *MagForce Nanotechnology* (hospital Charité in Berlin) [25–27] and with its use to enhance the sensitivity of tumour cells towards chemo- or radio-therapy, to trigger a thermally-induced release of drugs or to act on cell membranes [25–29]. However, one of MH limitations is the low heating power of most magnetic NPs, requiring a local injection of large quantities of NPs. Given the clinical importance of these results, there is currently a crucial need to design optimized NPs for efficient MH [30, 31]. NPs with magnetic properties specifically tailored for hyperthermia related applications [30, 32–34] is thus currently a key challenge to overcome in synthesis. Size is a factor with an optimum size for this application reported around 20 nm for spherical magnetite NPs [35]. But the key parameter in the NP design is the magnetic anisotropy and one way to increase it is to modify shape anisotropy [36–38]. The increase of SAR observed by controlling the shape as observed for cubic iron oxide NPs [39], nanoflowers [40] or rods [41, 42] show the interest of this strategy.

However, the heating efficiency of magnetic NPs depends also on the magnitude ( $H$ ) and frequency ( $f$ ) of the applied magnetic field [5, 7]. Indeed the heating performance is usually assessed by determining the specific absorption rate (SAR) which is the power dissipated by magnetic NPs per unit of mass [43]:  $SAR = C/m \times dT/dt$  with  $C$ , the water specific heat per unit of volume,  $m$  the iron oxide concentration in suspension ( $g\ l^{-1}$ ) and  $dT/dt$  the increase in measured temperature. SAR (in  $W\ g^{-1}$ ) values depend on the structure and composition of the NPs. For an efficient heat treatment with minimal invasiveness for the patient, the search for new magnetic nanomaterials which show the highest SAR values at the lowest NPs dose administered with the lowest frequency and/or magnetic field amplitude applied is of paramount relevance [30, 31, 39, 44].

Finally, it is important to consider cell internalisation. MH treatment can be applied providing that a sufficient amount of NPs is internalized. Among parameters for cellular uptake are particle size and shape. Smaller particle sizes have been shown to yield more internalisation [45]. Several reports

[46] have observed an effect of the anisotropic shape of nano-objects. It has been suggested that, as the specific surface is higher for anisotropic NPs, there is more multivalent ionic interaction with the cell membrane leading to a higher internalisation. Shape control might therefore also offer an interesting approach to improve cell uptake.

In that context, our strategy was to tune the shape of the NPs to maximize their efficiency for both MRI imaging and MH treatment and to coat them with dendrons. We have previously reported the synthesis of various anisotropic shapes (cubes, plates and octopods) [47, 48]. Here, NPs with different morphology were functionalized with a dendron molecule leading to good colloidal stability in water, with the exception of nanocubes, which formed aggregates. All shapes presented high relaxivity values ( $r_2 > 200 \text{ mM s}^{-1}$ ), which varied with the NP shape. The relevance of our strategy for MRI is further confirmed with ghost images at 3 T. SAR measurements indicated that high heating was possible if the shape anisotropy is good enough. As we have previously demonstrated that the NPs synthesized with thermal decomposition present different phase of oxide between the core ( $\text{Fe}_{3-x}\text{O}_4$ ) and the surface ( $\text{Fe}_2\text{O}_3$ ) [49], we will express the SAR in  $\text{W g}^{-1}$  of iron to avoid approximation on the mass of oxide.

Then, when the cytotoxicity was assessed, *in vitro* tests were performed to measure the internalisation degree depending on the shape. The biodistribution of dendronized NPs displaying different shapes was investigated by *in vivo* MRI. Finally, magnetic hyperthermia was performed on cells loaded with NPs.

## 2. Experimental conditions

### 2.1. Dendronized NPs preparation

Syntheses of iron oxide NPs with various shapes and coated with oleic acid (OA) was achieved according to previously reported procedures [47]. Also, the synthesis procedure of the dendron molecule can be found in [18, 34, 50]. Functionalization of the NPs by the dendron molecules is performed through a direct grafting process. Typically for standard 10 nm sized nanospheres (NS), a suspension of 1 ml of NP@OA in THF ( $5 \text{ mg ml}^{-1}$ ) was let in contact with 7 mg of dendron in 4 ml of THF. The mixture was magnetically stirred during 24 h. The NP@dendron were then precipitated by addition of hexane followed by centrifugation ( $8000 \text{ rpm min}^{-1}$ , 3 min). The supernatant was discarded, and the NPs were easily dispersed in 10 ml DI water. This standard protocol was adapted depending on the shape. For all shapes, the concentration of NPs was decreased to  $0.25 \text{ mg ml}^{-1}$  by increasing the NP solution to 20 ml. Moreover, reaction time was optimized for each shape. Contact time for 20 nm NS was increased to 48 h. The three other shapes were grafted with a two-step process. After 48 h, for the plates (NPI) and the octopods (NO), and after 96 h for the cubes (NC), the solutions were purified by ultrafiltration to remove free oleic acid. After 3 steps of purification, the NPs were let in contact with 7 mg of dendron for the same time as the

first step. The grafted NPs were then purified from the ungrafted dendron molecules by ultrafiltration. After at least 4 purification steps, the pH of the NPs suspensions was adjusted to 7.4 and the suspensions were ready for characterizations.

The NPs were characterized by transmission electron microscopy (TEM) with a JEOL 2100 microscope (JEOL, Tokyo, Japan) operating at 200 kV (point resolution 0.18 nm) for morphology and size. Mean size of NPs and their size distribution were determined from the size measurements of more than 300 NPs using ImageJ software (NIH, Bethesda, MD, USA). The error presented corresponds to the mean diameter standard deviation determined from all these size measurements. For anisotropic NPs size measurement was performed on the side for nanocubes and nano-octopods; for plates the longer length of the hexagon face was measured along the thickness.

The stability of the functionalized NPs suspensions was assessed by dynamic light scattering (DLS) using a nano-size MALVERN zetasizer. Particle size distributions in water and in 150 mM NaCl were assessed at pH 7.4. Standard Infrared spectra were recorded between 4000 and  $400 \text{ cm}^{-1}$  with a Fourier transform infrared (FTIR) spectrometer, Spectrum 100 from Perkin Elmer (Perkin Elmer, Waltham, MA, USA). Samples were gently ground and diluted in non-absorbent KBr matrices.

The x-ray diffraction (XRD, Bruker, Billerica, MA, USA) pattern was recorded at room temperature with a Bruker D8 Advance diffractometer equipped with a monochromatic copper radiation source ( $K\alpha = 0.154056 \text{ nm}$ ) and a Lynx-Eye detector in the  $27^\circ$ – $65^\circ$  ( $2\theta$ ) range with a scan step of  $0.03^\circ$ . High purity silicon powder ( $a = 0.543082 \text{ nm}$ ) was systematically used as an internal standard. Profile matching refinements were performed through the Fullprof programme [18] using Le Bail's method [51] with the modified Thompson–Cox–Hasting pseudo-Voigt profile function.

Hysteresis cycles at room temperature of as synthesized NPs were performed with a Superconducting Quantum Interference Device (Quantum Design MPMS3).  $50 \mu\text{l}$  of known concentration suspensions of NPs are evaporated in a capsule; this step is repeated until a homogeneous layer of dried NPs covers the bottom of the capsule.

### 2.2. MRI experiments

**2.2.1. Relaxivity measurements.**  $T_1$  and  $T_2$  relaxation times measurements of dendronized IONPs were performed on a Bruker Minispec 60 (Karlsruhe, Germany) working at a Larmor frequency of 60 MHz (1.41 T) at  $37^\circ\text{C}$ . The longitudinal ( $\mathbf{r}_1$ ) and transverse ( $\mathbf{r}_2$ ) relaxivity values were obtained according to the general equation of relaxivity  $\mathbf{R} = \mathbf{R}_0 + \mathbf{r} \times [\text{CA}]$ , where [CA] is the concentration of the CA (i.e.) the concentration of Fe in IONPs,  $\mathbf{R}$  is the relaxation rate ( $1/T$ ) in the presence of the CA,  $\mathbf{R}_0$  is the relaxation rate of the aqueous medium in the absence of the CA and  $\mathbf{r}$  is the relaxivity value of the CA.

**2.2.2. In vitro images.** *In vitro* images were acquired on a clinical MRI (GE Signa HDxt 3 T, GE Healthcare, Milwaukee, USA) with a field of 3 T.  $T_1$  images were acquired with a spin

echo sequence (TR = 400 ms, TE = 10 ms) and the  $T_2$  images were acquired with a fast spin echo sequence (TR = 2 s, TE = 52 ms).

### 2.3. Cell studies

**2.3.1. Cell.** Human hepatocarcinoma Huh7 cells were propagated in Dulbecco's modified Eagle's medium supplemented with 10% of decomplexed foetal bovine serum, 0%, 5% penicillin and 0%, 5% non-essential amino acids.

**2.3.2. MTT assay.** The number of viable cells after exposure to dendronized NPs was evaluated by the MTT (3-[4,5-methylthiazol-2-yl]-2,5-diphenyl-tetrazolium bromide) assay. Huh7 cells ( $1.10^4$  cells per well) were seeded in a 96-well plate and incubated (37 °C and 5% CO<sub>2</sub>) overnight for attachment. The next day, the medium was replaced with fresh medium with various concentrations of dendronized NPs (1, 2, 4, 8 and 16 mM iron) diluted in complete culture medium and cells were allowed to grow for 24 h. After incubation time, the medium was discarded and the wells were thoroughly washed with 200  $\mu$ l of phosphate buffered saline (PBS) to eliminate all remaining extracellular NPs. 200  $\mu$ l of cell culture medium + MTT (0.5 mg ml<sup>-1</sup>) was added to each well and cells are incubated for further 3 h 30 at 37 °C and 5% CO<sub>2</sub>. After incubation time, the medium was carefully discarded and 100  $\mu$ l of DMSO was added to each well and incubated 15 min at room temperature under orbital shaking. Colour developed after the reaction was measured at 550 nm using Xenius microplate reader (SAFAS, Monaco). Cell viability percentage was calculated as the ratio of mean absorbance of triplicate readings of sample wells ( $A_{\text{sample}}$ ) compared to the mean absorbance of control wells ( $A_{\text{control}}$ ). DMSO was used as negative control,  $A_{\text{DMSO}}$ , as shown in the following equation.

$$\text{Cell viability} = \frac{A_{\text{sample}} - A_{\text{DMSO}}}{A_{\text{control}} - A_{\text{DMSO}}} \times 100\%. \quad (1)$$

**2.3.3. Flow cytometry.** Huh7 ( $2.10^5$  cells per well) were seeded in a 24-well plate (Greiner, Dominique Dutscher, ref 165305) and incubated (37 °C and 5% CO<sub>2</sub>) overnight for attachment. The next day, media was replaced with 1 ml per well of fluorescently labelled (Alexa 595, Dyomics) NP diluted in complete medium and cells were allowed to grow for 24 h at 37 °C in 5% CO<sub>2</sub>. Cells were then thoroughly rinsed with 1 ml of cold PBS. Cells were then incubated with 300  $\mu$ l of trypsin/EDTA solution (GIBCO, Ref R001100, Thermofisher) for 5 min. After incubation, 500  $\mu$ l of PBS were added and cells were harvested by centrifugation at 1000 rpm for 5 min. Cells were resuspended in 1 ml PBS + 2% paraformaldehyde (PFA) and kept at 4 °C protected from light until analysis. Cell fluorescence was analysed by flow cytometry using a FACS flow cytometer (Navios Flow Cytometer, Beckmann Coulter) with Novios software. Cells were analysed in FL1 channel (Exc 488 nm Em 505 nm). Fluorescence threshold was determined using non-treated cells. 10 000 cells were analysed per sample. For the magnetofection, neodymium boron iron disc magnets (0.8 mm

diameter, 0.8 mm height, strength 24.5 N, Supermagnete) were placed under the wells (with a distance magnet cells of about 1 mm). NP diluted in complete medium was introduced in the wells and let for 5 min. Then, the medium was removed, cells were rinsed with 1 ml PBS and fresh cell culture media was introduced. Cells were then incubated for 30 min at 37 °C in 5% CO<sub>2</sub>. Preparation for flow cytometry is similar to above.

**2.3.4. ICP-AES iron quantification in cells.** For iron content determinations, samples (cells were digested with concentrated nitric acid at 100 °C for 2 h. A blank test was carried out in parallel under the same conditions using the same reagents quantities. Analysis of iron in the digested samples were realized by ICP-AES (Varian 720ES) at 238 204 nm. Quantification was done with a calibration curve established with standards (0, 2, 10, 50, 100, 200, 500  $\mu$ g l<sup>-1</sup>) prepared using a certified standard. TraceMetal grade HNO<sub>3</sub> 67%–69% for cells and organs digestion was purchased from Fischer Chemical. A 1000 mg l<sup>-1</sup> iron certified standard (CPI International) was used to prepare standard solutions for ICP-AES analysis.

### 2.4. In vivo experiments

31 Mice were used for the biodistribution. Groups of three mice (four for nanoplates) were used per condition (shape of the NPs and time). Mice were anesthetized by inhalation of isoflurane vaporized in oxygen. The experiments were performed on a 400 MHz (9.4 T) Bruker Biospec imaging system according to the procedure accepted by the ethical committee of the centre for microscopy and molecular imaging (project CMMI-2011–07). The CA was injected intravenously at a dose of 45  $\mu$ mol [Fe]/kg body weight to female CD-1 mice (5–10 weeks old, from Charles River Laboratories (France)). First sequence of imaging was started close to the injection time and scans were performed up to 4 or 24 h. The signal intensity (SI) was measured in the regions of interest (ROIs) drawn on the liver and the bladder, and in an external reference tube. The SI enhancement ( $\Delta$ SI%) was calculated according to the following equation, where  $SI_{\text{post}}$  = post-contrast and  $SI_{\text{pre}}$  = pre-contrast SI.

$$\Delta SI\% = \left| \frac{SI_{\text{post}} / \text{ref} - SI_{\text{pre}} / \text{ref}}{SI_{\text{pre}} / \text{ref}} \right| \times 100.$$

### 2.5. Magnetic hyperthermia

**2.5.1. In solution.** Magnetic hyperthermia in solution was measured on a DM1 apparatus from Nanoscale Biomagnetics™. Aqueous NPs suspensions were placed for 5 min in the apparatus for temperature equilibration. The samples were subjected to the alternating magnetic field (395 or 795 KHz, 12 kA m<sup>-2</sup>) until temperature plateau was achieved.

**2.5.2. In vitro.** Huh-7 cells were seeded in a 9.3 mm petri dish at a concentration of  $1.10^5$  cell per well. Then cells were incubated with complete medium and kept overnight for attachment at 37 °C in 5% CO<sub>2</sub>. Cells were then incubated, with 2 ml per well of NP diluted in complete medium, for 24 at 37 °C in 5% CO<sub>2</sub>. Cells were then thoroughly rinsed with



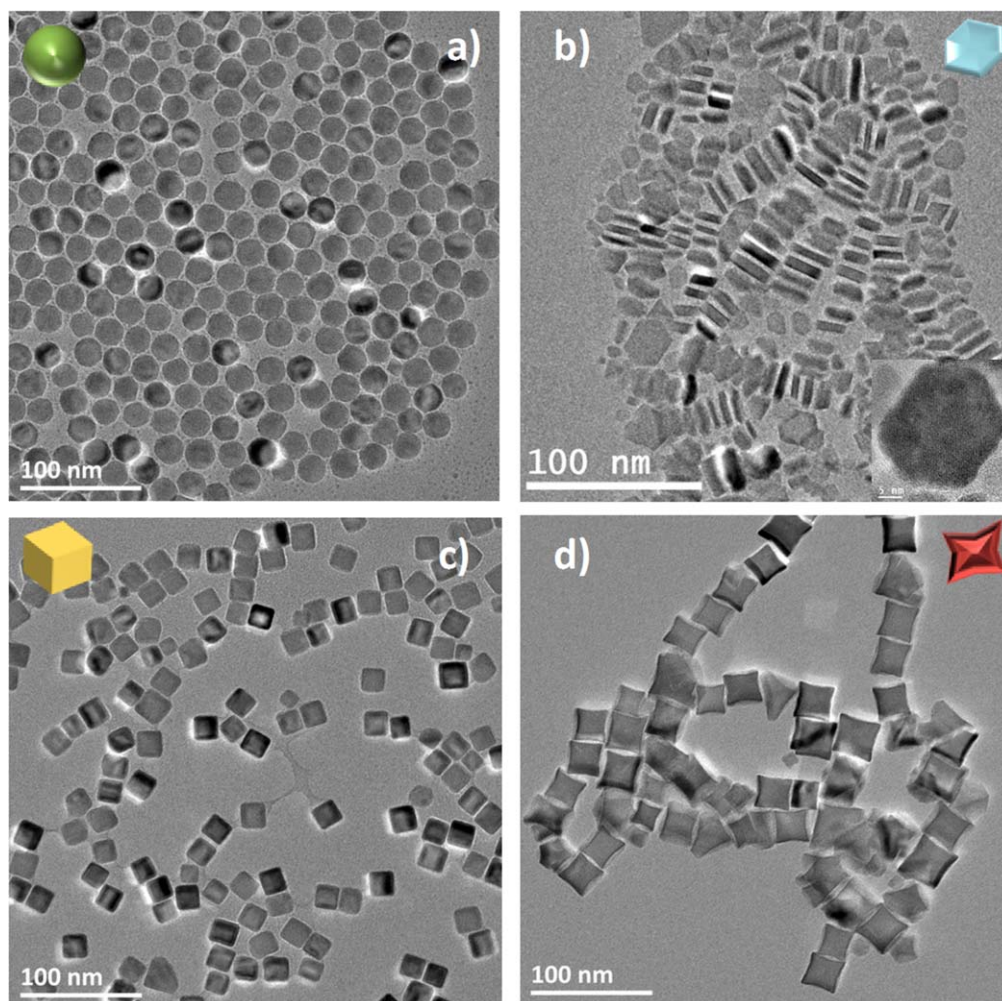


**Figure 1.** TEM images of (a) NS, (b) NPI, (c) NC and (d) NO.

2 ml of cold PBS and 2 ml of complete medium with 25 mM HEPES was added. The dishes with the cells monolayers were introduced in the magnetic hyperthermia apparatus (nanoscale biomagnetic DM3) and were treated with a 401 KHz and  $13 \text{ kA m}^{-2}$  homogenous magnetic field for 50 min on a magnetic hyperthermia apparatus. Control experiments were performed with cells monolayers kept at  $37^\circ\text{C}$  or in the apparatus without application of the magnetic field. After the treatment, cell monolayers were then dyed for cell death detection with the Apoptic/necrotic/healthy cells detection kit (PromoKine). Fluorescence images were captured using Nikon Elipse TE200 with  $63 \times \text{PL APO}$  (1.4 NA) objective equipped with Nikon Digital Camera (DS-Q11MC with NIS-Elements software) and processed with ImageJ (<http://rsb.info.nih.gov/ij/>).

### 3. Results

#### 3.1. Preparation and characterization of dendronized NPs

Iron oxide NPs with various morphologies were synthesized through the thermal decomposition process. Four shapes with

a mean size around 20 nm were obtained: spherical NPs (NS) (isotropic reference) and three anisotropic shapes, nanocubes (NC), nanoplates (NPI) and nano-octopods (NO). Details on the formation and shape control for NC, NPI and NO can be found in [47, 51] and for NS in ref (submitted). Transmission electron microscopy (TEM) images of the spheres (NS), cubes (NC), octopods (NO) and plates (NPI) are shown in figure 1 and their main structural properties are summarized in table 1 and in figure S1 (available online at [stacks.iop.org/NANO/30/374002/mmedia](http://stacks.iop.org/NANO/30/374002/mmedia)). Size distribution of the different NPs are presented in figure S1.

All the synthesized NPs present a spinel structure close to the magnetite  $\text{Fe}_{3-x}\text{O}_4$  composition except NC that displays a core-shell  $\text{Fe}_{1-x}\text{O}@\text{Fe}_{3-x}\text{O}_4$  composition, as previously described [47, 48, 51] and proved from the analysis of XRD pattern (figure S1). The saturation magnetisation  $M_s$  of the NPs is one of the major parameter to consider for their use as MRI contrast enhancers, with obtained values showing  $M_s$  changes as  $\text{NS} > \text{NO} > \text{NPI} > \text{NC}$ . The low  $M_s$  for the plate can be explained by the flat thin shape that implies a large surface/volume ratio that should favour spin canting at the surface lowering thus the  $M_s$ . The  $M_s$  for nanocubes is difficult to calculate because they show a core-shell structure with

**Table 1.** Main structural parameters of the different shaped NPs deduced from TEM (mean size), XRD (composition) and magnetic measurements ( $M_S$ ).

NPs	Mean TEM size (nm)	Composition	$M_S$ (emu/g <sub>Fe<sub>3</sub>O<sub>4</sub></sub> )
NS	22.2 ± 1.8	Fe <sub>3-x</sub> O <sub>4</sub>	69 ± 5
NC	14.5 ± 1.6	Fe <sub>1-x</sub> O@Fe <sub>3-x</sub> O <sub>4</sub>	39 ± 5
NO	27.8 ± 4.2	Fe <sub>3-x</sub> O <sub>4</sub>	58 ± 5
NPI	16.7 ± 5.2 (length) 5.7 ± 1.6 (thickness)	Fe <sub>3-x</sub> O <sub>4</sub>	43 ± 5

an antiferromagnetic core which does not contribute to  $M_S$  at room temperature.

At the end of the thermal decomposition synthesis, the NPs are coated with the hydrophobic ligands introduced for the synthesis (oleic acid (OA) and stearate and/or oleate) that ensure their colloidal stability in organic solvent. The obtained particles are rendered biocompatible by exchanging the surfactants from the surface with a hydrophilic dendron molecule by direct exchange in THF, as previously reported for 10 nm spheres [17, 18, 52]. Moreover, we have previously demonstrated that the functionalization with the dendron molecule using phosphonate anchoring groups tend to passivate the NPs preventing them from a further oxidation [34, 52] and thus preserving their composition.

The success of the ligand exchange is first assessed by FTIR spectroscopy [18, 21, 52]: the IR spectrum of the NPs after grafting (NPs@D2-2P) is compared to the spectrum of the NPs after synthesis (NPs@OA) and to the one of the D2-2P molecule (figure S2). The IR spectrum of the D2-2P molecule presents several P–O bands with a P=O band appearing at 1200 cm<sup>-1</sup> and P–OH bands at 1027 and 995 cm<sup>-1</sup> [21–23, 53]. An intense C–O–C band is detected at 1110 cm<sup>-1</sup> and the C=O band appears at 1700 cm<sup>-1</sup>. After the grafting step, the carboxylate bands observed in the NP@OA at around 1500 and 1400 cm<sup>-1</sup> are replaced with the C=O band of the D2-2P at 1700 cm<sup>-1</sup> and N–CO at 1640 cm<sup>-1</sup>. The alkyl chain bands at 2900 and 2800 cm<sup>-1</sup> have almost completely disappeared. The C–O–C and the P=O bands are not observed such as P–OH bands due to the formation of the P–O–Fe (992 cm<sup>-1</sup>) bonds [23]. The disappearance of those bands indicated a strong coordination of the dendron at the NPs surface through the phosphonate anchoring group.

The colloidal stability in water and in iso-osmolar media (150 mM NaCl) has been evaluated by DLS (figure 2). The mean hydrodynamic size determined either in water or NaCl is given in table 2. This value is only indicative of potential aggregation for shapes other than NS as the optical model used to calculate the size distribution considers spherical NPs. Anisotropic NC, NO and NPI may be present in front of the laser under different orientations that can be longer than the edge length or the diameter. Therefore, the values of mean hydrodynamic diameter are just given for comparison and cannot be considered as accurate.

The mean hydrodynamic size in water of dendronized NS was determined at about 28 nm, slightly larger than the TEM

size of NPs (22 nm) but consistent with the dendron coating (thickness of 1.5–2 nm) and the solvation layer: it confirms that no aggregation occurs during the dendronization step. The measurement in NaCl indicated no sign of aggregation with a monomodal hydrodynamic size distribution and a slightly higher mean diameter remaining below 50 nm. NPI and NO present a good stability in both media with quite a monomodal distribution and a small second population above 100 nm. As this second population is not observed for both media (H<sub>2</sub>O and NaCl 150 mM), we suspect that it originates less from aggregation than from the measurement of several NPs at once. On the opposite, NC present a clear sign of aggregation with a multimodal size distribution with the presence of an intense peak around 5000 nm indicating a lower stability after the functionalization with the dendron. The difficulty in dendronization of nanocubes has already been reported and attributed to their flat faces which favour a close packed monolayer of oleate molecules affecting strongly their exchange [34]. Similar difficulty of functionalizing anisotropic shapes has been reported for rods [54]. For *in vitro/in vivo* experiments, all the suspensions were filtrated (0.22 μm pores filter unit) to eliminate potential large aggregates.

### 3.2. $T_2$ relaxivity and MH properties of different shapes of iron oxide NPs

#### 3.2.1. Relaxivity measurements and magnetic hyperthermia.

Relaxivity measurements allow to evaluate the potential of nano-object to act as MRI CA. A good  $T_2$  CA shall display high  $r_2$  values and high  $r_2/r_1$  ratio [10]. In MRI, the main NPs parameters are the saturation magnetization ( $M_S$ ) and the size [55]. As the size is kept as almost constant for the different shapes the  $M_S$  may be considered as the predominant parameter. The higher the  $M_S$ , the higher the transverse relaxivity ( $r_2$ ) will be as demonstrated by Yoon *et al* [56]. Measurements were performed for all dendronized shapes at different field: 0.47 T (20 MHz), 1.41 T (60 MHz) and 7.04 T (300 MHz). The longitudinal  $r_1$  and transverse  $r_2$  relaxivity values are given in table 3.

Compared to commercial products [57] and dendronized 10 nm sized spheres [34], all the shapes presented very high transversal relaxivities ( $r_2$ ). Surprisingly, we did not observe an increase of the  $r_2$  values with increasing fields as described by Gillis who demonstrated that  $r_2$  should increase linearly with the field until a plateau when the saturation

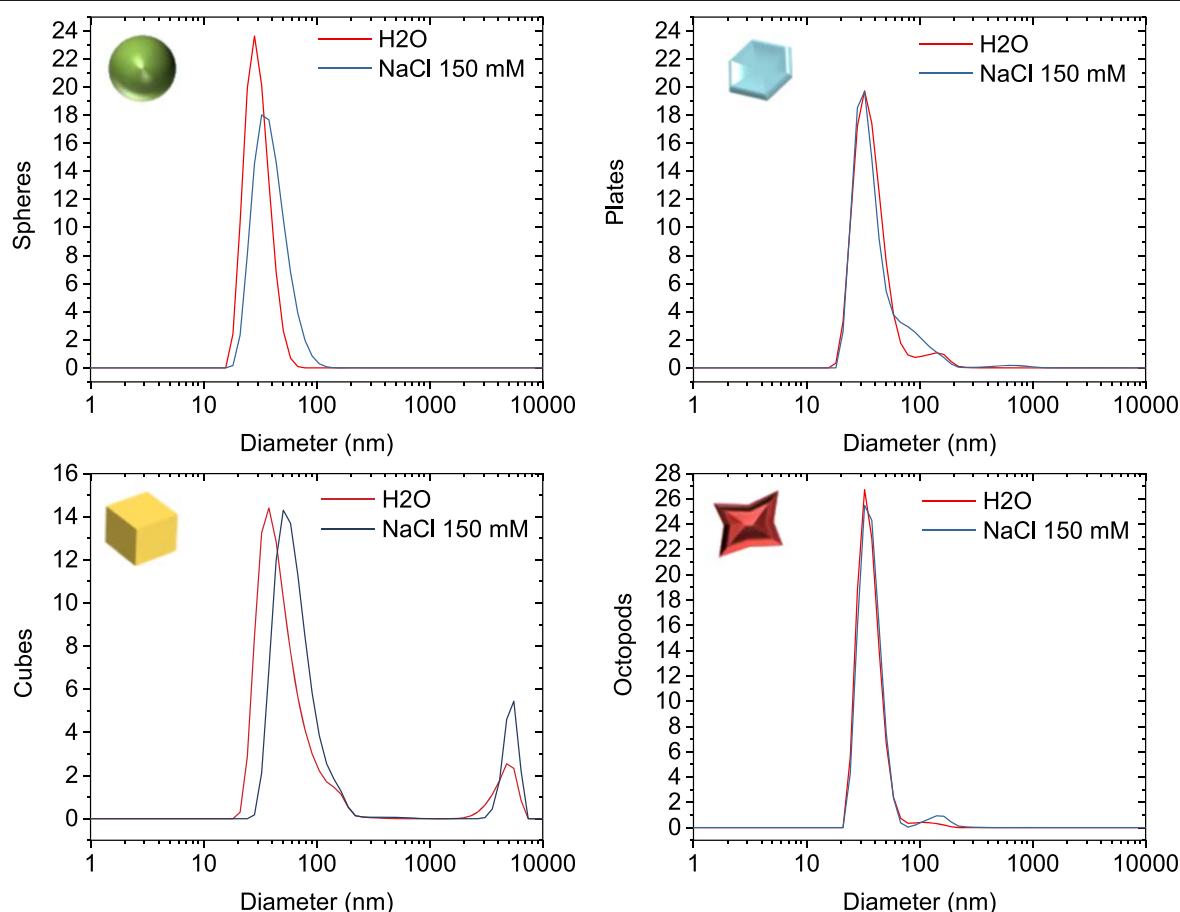


**Figure 2.** DLS measurements (volume) in H<sub>2</sub>O (red curve) and NaCl 150 mM (blue curve) for NS (a), NC (b), NPI (c) and NO (d).

**Table 2.** Mean hydrodynamic diameters of the NPs in various media.

Shape	Mean hydrodynamic diameter (nm)			
	In H <sub>2</sub> O		In NaCl 150 mM	
	Size	Pdi	Size	Pdi
NS	28	0.112	35	0.115
NC	38	0.568	50	0.601
NO	5500		5000	
	32	0.289	35	0.312
NPI			150	
	32	0.420	32	0.355
	150			

magnetization is reached [58]. We suppose that this saturation plateau is already reached at 0.47 T for the four shapes studied here, meaning that they have already reached their maximum  $r_2$  value at low field. NS presented a  $r_2$  value higher than NS10. NPIs showed  $r_2$  values in agreement with published ones [59] whereas NO presented lower  $r_2$  than previously reported ( $r_2 = 679.3 \pm 30 \text{ mM}^{-1} \text{ s}^{-1}$  at 7 T, edge length of 30 nm) [60] due to a lower  $M_S$ . NC displayed large  $r_2$  values compared to the  $M_S$  measured. This can be explained by the aggregation observed by DLS. Indeed, as reported [61–63], the aggregation state can boost the  $r_2$  values up to a maximum.

Comparing the  $r_2$  values for all shapes, we observe the impact of the shape anisotropy on the results. At 0.41 T, NS with a mean size of 22 nm present a  $r_2$  value of  $298 \text{ s}^{-1} \text{ mM}^{-1}$  four times larger than the value measured for the NS with a mean size of 10 nm. This is due to the increase of  $M_S$  with the size. But NO that presented a lower  $M_S$  than NS showed a comparable  $r_2$  value demonstrating the impact of the shape anisotropy. As suspected, NPI do not present a strong enough shape anisotropy to compensate their low  $M_S$  leading to the lowest  $r_2$  of the series. As detailed above, NC present a  $r_2$  value related to their aggregation state.

The same trend is noticed with SAR measurements on suspensions containing 18 mM in iron and with a frequency of 795 KHz and magnetic field amplitude of  $12 \text{ kA m}^{-2}$  (table 3). The SAR value with NO is larger than that of NS. As the SAR value difference is larger here than for relaxivity values, we hypothesize that the NO shape promotes a local organization of the NPs through the formation of chains resulting from dipolar coupling leading to anisotropy increase/hysteretic losses [64, 65]. That hypothesis is supported by the observed spontaneous alignment of octopods in TEM image in figure 1. The lowest SAR value of the series obtained for NC confirms that the high  $r_2$  value was due to their aggregation state. At a lower frequency (395 KHz) close to the highest one achievable when using the *in vitro* hyperthermia apparatus, only NS and NO present a



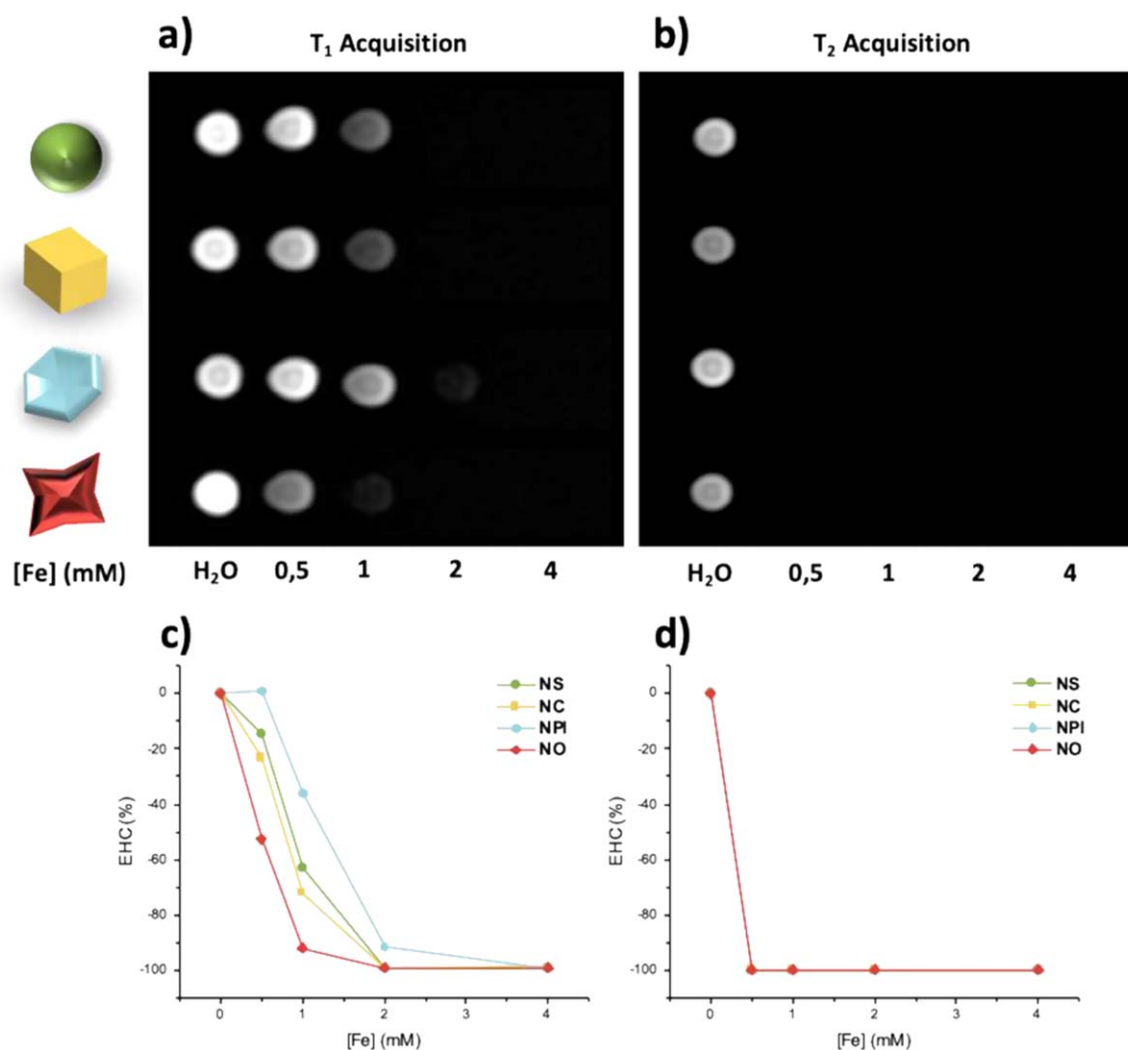


**Figure 3.** Ghost images at 3 T,  $T_1$  acquisition (a) and  $T_2$  acquisition (b) and EHC evolution with the concentration in iron for the  $T_1$  (c) and  $T_2$  (d) acquisition.

**Table 3.** Relaxivity values of all  $T_2$  dendronized NPs at 0.47, 1.41 and 7.04 T.

At 37 °C	Mean diameter (nm)		Relaxivity at 0.47 T (s <sup>-1</sup> mM <sup>-1</sup> )			Relaxivity at 1.41 T (s <sup>-1</sup> mM <sup>-1</sup> )			Relaxivity at 7 T (s <sup>-1</sup> mM <sup>-1</sup> )			SAR (W/g <sub>Fe</sub> ) at 1 mg ml <sup>-1</sup> Fe	
	TEM	DLS	$r_1$	$r_2$	$r_2/r_1$	$r_1$	$r_2$	$r_2/r_1$	$r_1$	$r_2$	$r_2/r_1$	395 kHz 12 kA m <sup>-1</sup>	796 kHz 12 kA m <sup>-1</sup>
Resovist	3–5	62	25.4	152	5.9	9.7	189	19.5	ND	ND	ND	ND	ND
NS10 <sup>a</sup>	10	18	31	76	2.5	13	78	6	ND	ND	ND	0	0
NS	22.2 ± 1.8	28 <sup>b</sup> 0.112	42	298	7	10	303	32	0.6	300	515	120 ± 14	395 ± 20
NC	14.5 ± 1.6	38 <sup>b</sup> 0.568	41	356	9	11	332	30	0.8	309	487	0	177 ± 18
NPI	16.7 ± 5.2	32 <sup>b</sup> 0.420	43	212	5	13	198	15	1.1	186	169	0	238 ± 16
NO	27.8 ± 4.2	32 <sup>b</sup> 0.289	42.5	306	7.2	8	274	34	0.5	295	590	200 ± 12	462 ± 28

<sup>a</sup> Values from Walter *et al* [34].

<sup>b</sup> PDI values.

significant macroscopic heat increase allowing SAR value determination.

**3.2.2. In vitro images.** Ghost images of the different NPs suspensions were acquired on an MRI scanner equipped with

a 3 T magnet at room temperature. The acquisitions allowed a visual assessment of the contrast enhancement and the determination of the enhancement contrast ratio (EHC). The EHC allows determining the concentration of NPs at which the signal extinction in order to compare the different shapes.

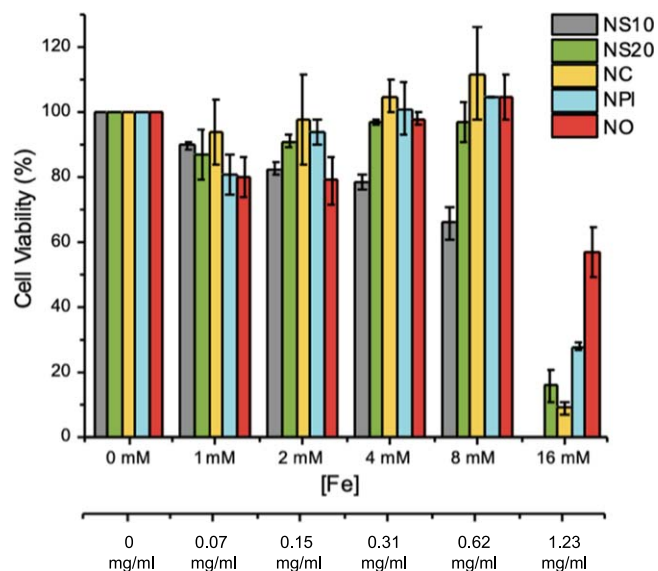


**Figure 4.** Cell viability of Huh-7 cell monolayer as a function of the NPs shapes, 10 nm spheres (grey), 20 nm spheres (green), cubes NC (yellow), plates NPI (blue) and octopods NO (red) as function of concentration in iron (mM) or iron oxide ( $\text{mg ml}^{-1}$ ).

EHC is defined as follows:

$$\text{EHC}_{\text{sample}} = \frac{S_{\text{sample}} - S_{\text{water}}}{S_{\text{water}}} \times 100$$

with  $S_{\text{sample}}$  and  $S_{\text{water}}$  the intensity of the sample and water respectively.  $T_1$  and  $T_2$  weighted ghost images and EHC evolution are given in figure 3.

Ghost images performed at 3 T confirmed a strong  $T_2$  behaviour for all shapes as noticed with the previous relaxivity measurements.  $T_2$  weighted ( $T_{2w}$ ) ghost images showed a massive hypo-contrast even at low concentration (0.5 mM).  $T_{2w}$  EHC indicated that, for all shapes, the extinction was complete ( $-100\%$ ) with the smallest investigated concentration of iron (0.5 mM).  $T_1$  weighted ( $T_{1w}$ ) acquisitions presented a difference in behaviour depending on the shapes. For all NPs, a hyposignal in  $T_{1w}$  images is observed: this effect is very weak at low iron concentrations and increases as the iron concentration increases. This evolution is shape dependant. At low concentration (0.5 mM), NO presented the largest loss in signal ( $-52.7\%$ ). NC ( $-23.3\%$ ) and NS ( $-14.6\%$ ) values were intermediate when NPI presented a weak hypersignal ( $+0.95$ ). This may be explained by the large (111) surface exposed by NPI. Indeed, those faces are Fe rich thus promoting  $r_1$  relaxation. This  $r_1$  relaxation can be ascribed to the interaction of water molecules with the iron atoms of the surfaces in an ‘inner sphere mechanism’ prevailing over the ‘outer sphere mechanism’ (at distance, through dipolar interactions between the nuclear and electron spins).

Afterwards, with an increasing iron concentration, the  $T_{1w}$  EHC dropped for all morphologies while keeping the same trend. By 2 mM, all shapes except NPI ( $-91.8\%$ ) were extinct. The extinction for all shapes is complete at 4 mM. The strong  $T_{1w}$  shortening at high concentration can be

related to the strong  $T_2$  shortening and also to a NPs clustering favoured at such high concentration [61, 66].

### 3.3. Biological studies

**3.3.1. Cell viability.** Cell viability has been assessed (figure 4) in order to ensure that the different shapes are safe for further *in vivo* studies. At 24 h no NPs, no matter their shape, show any sign of cytotoxicity up to 8 mM. At 16 mM, cell mortality was detected and showed a shape dependence with NC and NS leading to the highest cell mortality. The variation of cell mortality with the shape could be explained either by the fact that as the volume of a single NP vary for each shape, the number of NPs will vary for a defined amount of iron or by a difference in the NPs internalization rate due to shape effect.

The cell viability observed here is in agreement with a former study on dendronized 10 nm spheres on different cell lines [24]. The low cell mortality can be explained by a low internalization of the NPs due to the antifouling effect of the dendritic coating [24]. Comparing to other studies [67], the various morphologies present a low toxicity at higher concentrations than the ones tested in [67].

**3.3.2. NPs cell internalization study.** Cell internalization rates were studied as a function of the NPs shape in order to better understand the variation in cell viability observed above. We previously reported [24] that 10 nm dendronized spheres (NS10) showed no unspecific uptake by cells due to the dendron effect, similar to an antifouling effect. To get a qualitative and quantitative assessment of the internalization rate, different techniques were employed including flow cytometry.

To determine NPs internalisation using flow cytometry, Alexa 595 amine fluorophores were coupled on the carboxylic group of the D2-2P dendron molecule through EDC coupling. Those fluorescent NPs (NPs@D2-2P@Alexa) were incubated with Huh7 cells for 24 h and 48 h at several concentrations ranging from 0.5 to 2 mM in iron. Cells were analysed with FACS. In all analysis, cell debris and free particles were excluded by setting a gate on the plot of side-scattered light (SSC) versus forward-scattered light (FSC). The acquisition parameters were optimized for the Alexa 495 fluorophore with an excitation at 488 nm and detection above 505 nm. Non-treated Huh 7 cells were used to gate cell autofluorescence. Huh7 Particle internalisation was obtained from the fluorescence intensity difference between treated and non-treated cells. Interestingly, instead of seeing two populations (one with fluorescence intensity comparable to the control and one showing fluorescence intensity above control), a single population was detected with fluorescence intensity above the control. As all the population showed a shift of fluorescence intensity, it would imply that all the cells internalised NPs to some extends. Thus, instead of treating the percentage of fluorescent cell, the shift of the mean fluorescence was assessed.

Figure 5(a) shows the evolution of the fluorescence shift with NPs concentration. All shapes presented a shift increase as a function of NP concentration and incubation time. The most noticeable variation is observed for NC which would

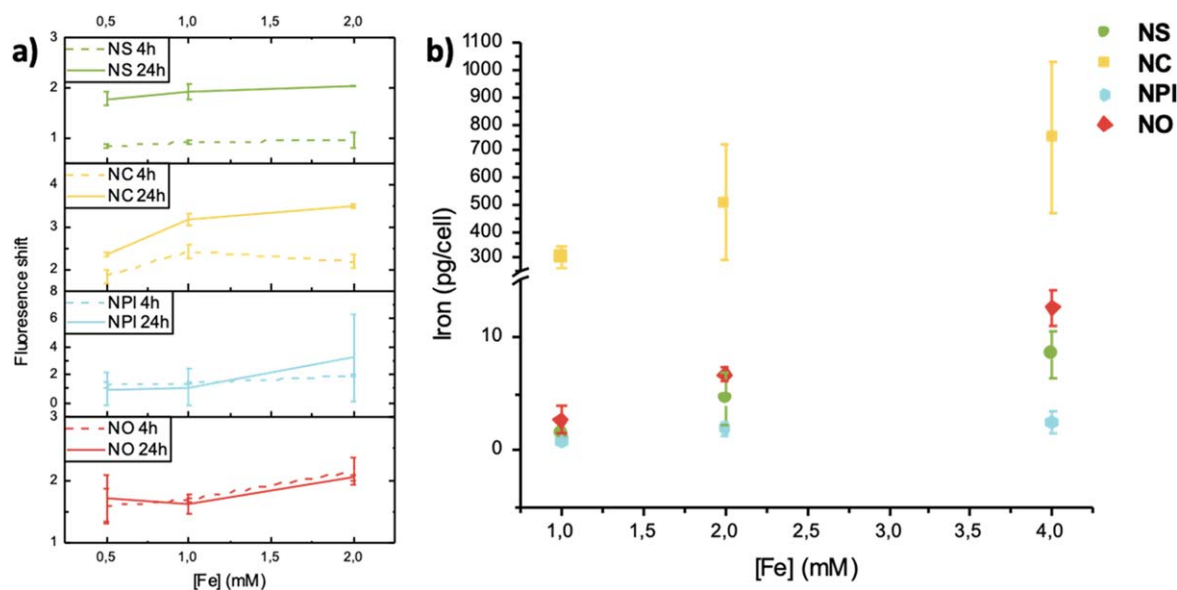


**Figure 5.** Fluorescence shift observed in flow cytometry for the shapes depending on incubation time and concentration (a) and Iron determination of cells after internalisation experiments subtracted from the endogenous level in iron in control cells (b).

suggest a higher internalization for this shape. Such an uptake has only been reported by Hémery *et al* [68] for multicore NPs and in our case can be explained by the trend for aggregation of the NC.

Yet, as the whole surface of each shape is different, they should present different individual fluorescence intensities depending on the number of fluorophores grafted on the surface and no quantitative comparison between different shapes can be done on their internalisation ability.

We have attempted to quantify the obtained flow cytometry shift by comparison with the amount of iron per sample. To get a sufficient amount of internalized NPs, we measure fluorescence intensity in Huh7 cell incubated with NS coupled with Alexa 595 that were internalized at different concentrations (0.6–9 mM) in Huh7 cells by magnetofection. After incubation for 24 h and washing, cells were counted, the iron was titrated with ICP-AES and the remaining part was used for flow cytometry measurements. Once again, we did observe a complete shift of the fluorescence. The shift of the mean fluorescence (i.e. mean fluorescence of the internalized cells—mean fluorescence of the non-internalized cells) was then plotted versus the amount of iron per cells (figure 6).

We observed an increase of the mean fluorescence shift with the intracellular iron concentration with cell uptake in agreement with previous report [69]. Above 0, 05  $\mu\text{g}$  of iron per cells, the variation is linear ( $R^2 = 0.998$ ). This result indicated that the study of the mean fluorescence shift is interesting when enough NPs are internalized ( $>0, 05 \mu\text{g}_{\text{Fe}}/\text{cell}$ ). Flow cytometry could be thus a quantitative method for the NPs internalisation. In our case, such calibration curve should be performed for each NPs in order to quantify internalisation and to be able to compare each system. However, this experiment confirmed that if the mean fluorescence shift value is higher, more NPs are internalized. Such kind of calibration curve should be hence

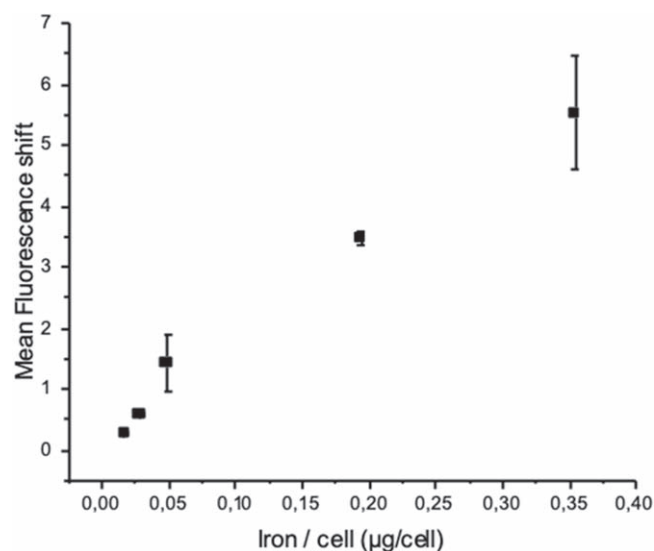


**Figure 6.** Mean fluorescence shift versus the amount of iron per cells after magnetofection of NS.

investigated and established for each morphology in future works.

The assessment of internalised NPs by ICP-AES provided a more quantitative understanding of the internalisation process. Figure 5(b) showed the evolution of the iron concentration (in pg/cell), subtracted from the endogenous iron level measured in control cells, as function of the iron concentration of the injected dose of NPs. The determination of iron confirmed that the number of internalized NPs increased with NPs concentration in accordance with flow cytometry results. It also confirmed that NC presented the largest internalization among all shapes. NS, NPI and NO showed an iron concentration below 10 pg/cell with a

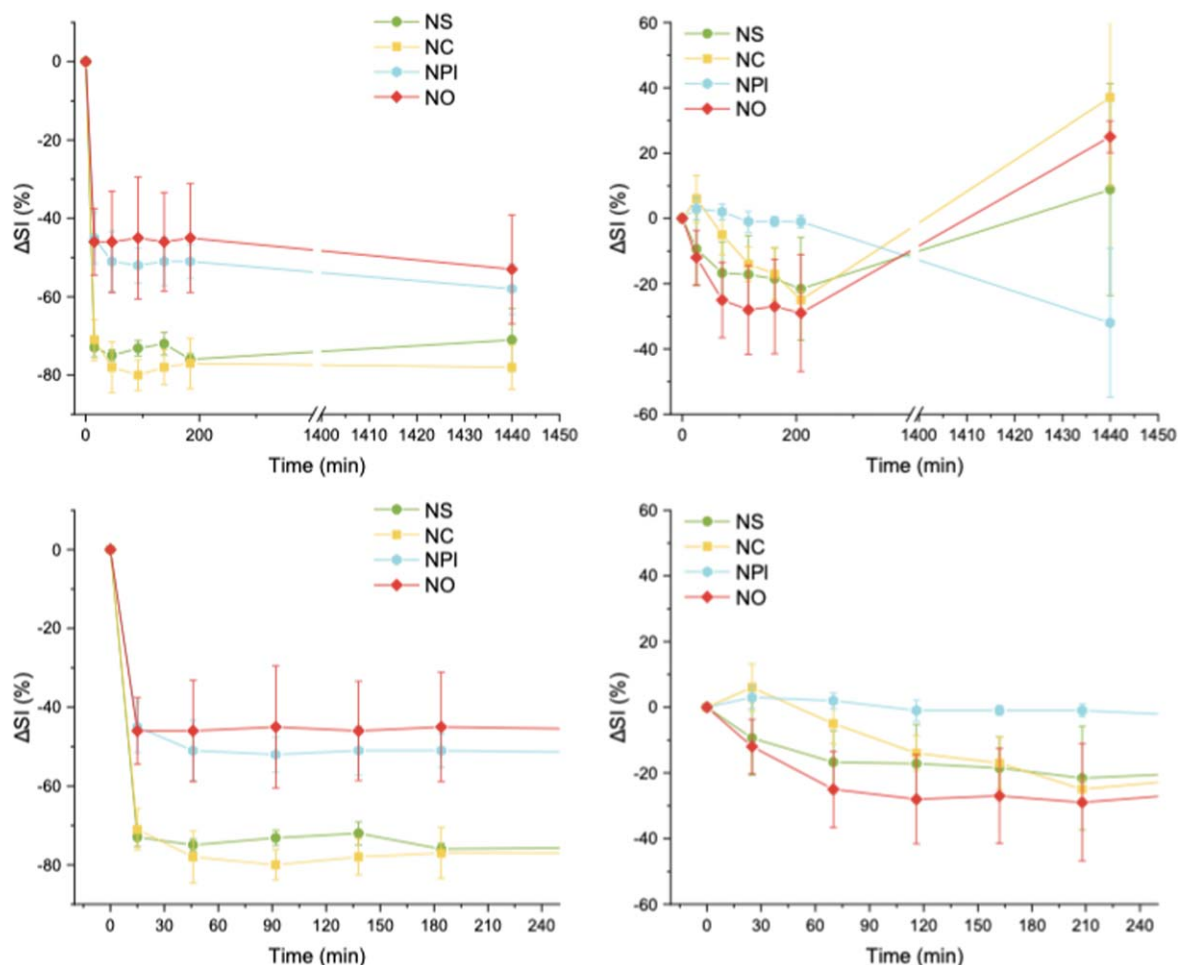


**Figure 7.**  $\Delta SI$  variation in the liver (left) and the bladder (right), bottom line shows a zoom focused on early timepoints.

difference more marked at higher concentration (4 mM). Interestingly the same trend than for relaxivity and magnetic hyperthermia is observed with  $C_{Fe,NO} > C_{Fe,NS} > C_{Fe,NPI}$ .

### 3.4. In vitro and in vivo

#### 3.4.1. Preliminary in vivo biodistribution by MRI.

Biodistribution of the four shaped NPs was followed by MRI. Mice were imaged before and at different times after injection (15 min, 45 min, 1h30, 2h20, 3 h and 24 h). Three mice per shape were imaged. They were then sacrificed and their organs harvested for iron quantification. Three mice were also injected with NPs and sacrificed 4 h after the injection (but not imaged) to get an insight of iron distribution closer to the injection time. *In vivo* MR images of mice acquired with slightly  $T_2$  weighted coronal spin echo sequence for liver (TR = 2000 ms, TE = 17 ms) and  $T_2$  weighted axial spin echo sequence for urinary bladder (TR = 7726 ms, TE = 52 ms) are shown in figures 10 and 11, respectively. The  $\Delta SI$  evolutions measured in the liver and in the bladder are shown in figure 7 and the evolutions in the renal pelvis and in the bladder are shown in figure 8. We observed a strong signal decrease in the liver already 15 min after injection for all shapes, which was confirmed with the

$\Delta SI$  measurement. The signal in the liver slightly varied afterwards but remained strongly attenuated. This indicated some capture of NPs by the liver. Previous observations on the biodistribution of dendronized 10 nm spheres [24] showed an evolution of the signal in the liver indicative of a transient passage of the NPs (without accumulation) over their metabolism. On the opposite, the evolution of the  $\Delta SI$  in the bladder suggested elimination also through urinary pathway during the first 3 h for all shapes except NPI. This was in agreement with the evolution of the  $\Delta SI$  in the renal pelvis (figure 8). However, the error was significant in the renal pelvis.

ICP-AES quantification on harvested and digested organs (figure 9) did not allow an accurate measurement of the amount of iron in various organs (liver, kidneys, lungs and bone marrow). Nevertheless, the measurements suggest a quite low accumulation in organs. The collected urine samples confirmed a strong urinary elimination; however, as the number of samples was too low, no statistical analysis could be done. For the signal in the liver, we suggest that, as the  $T_2$  effect is strong for all shapes, a small amount captured in the liver would induced a strong contrast constant with time.

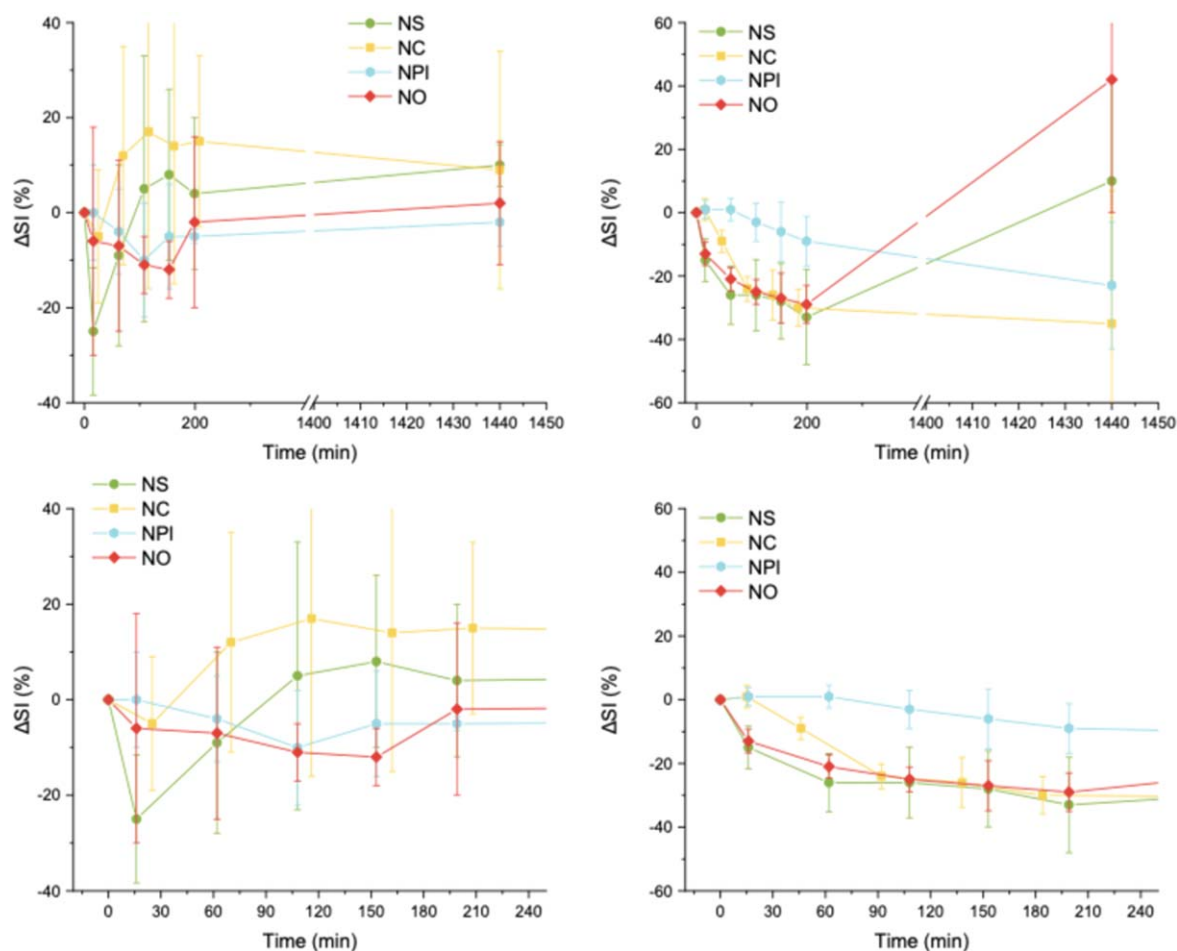


**Figure 8.**  $\Delta SI$  variation in the renal pelvis (left) and the bladder (right), bottom line shows a zoom focused on early timepoints.

The evolution of signals is here rather similar to that reported in our previous study with dendronized 10 nm sized spheres where a fast hepato-biliary, together with a low urinary eliminations were observed [24]. The urinary and hepato-biliary elimination kinetic was quite rapid with the small NPs and we may suppose that it is slower with these bigger NPs.

**3.4.2. MH *in vitro*.** NPs efficiency in magnetic hyperthermia (MH) was assessed for all shapes on Huh7 cells. NPs efficiency in hyperthermia therapy relies in two aspects: their ability to generate heat and their ability to enter cells. In both aspects, size, shape and concentration are fundamental. Yet, due to the dendron molecule on the surface of the NPs, cell internalization is weak. In order to get a preliminary result on the efficiency of the differently shaped nano-objects, hyperthermia treatment was performed both on cells incubated with NPs and on cells after magnetofection to insure NP cell internalization. Before MH treatment, cells were washed thoroughly with PBS and medium was replaced by fresh culture medium +10 mM HEPES. The alternating magnetic field was applied for 50 min (400 KHz, 13 k A m<sup>-2</sup>). Then, cells were incubated at 37 °C in 5% CO<sub>2</sub> for 24 h. After incubation time, cells were fixed with PFA 4% at room temperature for 15 min. Cells were labelled with annexin V and ethidium homodimer III to detect apoptotic

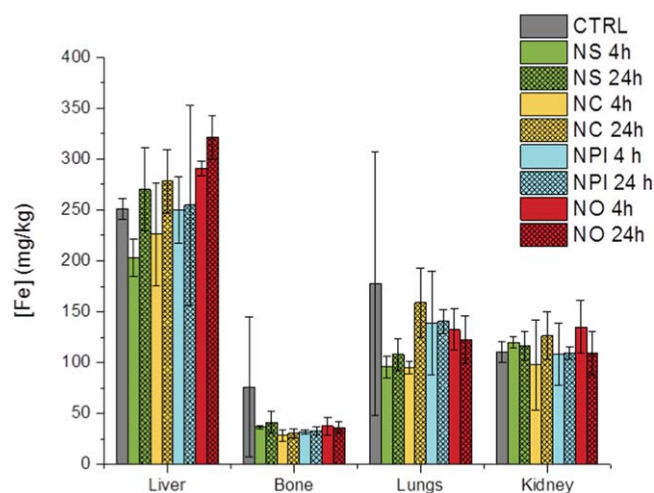


**Figure 9.** ICP-AES iron quantification in various organs.

and necrotic cells, respectively. The percentage of apoptotic and necrotic cells were determined from epifluorescence microscopy images (figures 12 and 13).

The percentage of necrotic and apoptotic cells observed was low (<20%) with a large standard deviation, especially for the magnetofection group. This is due to the



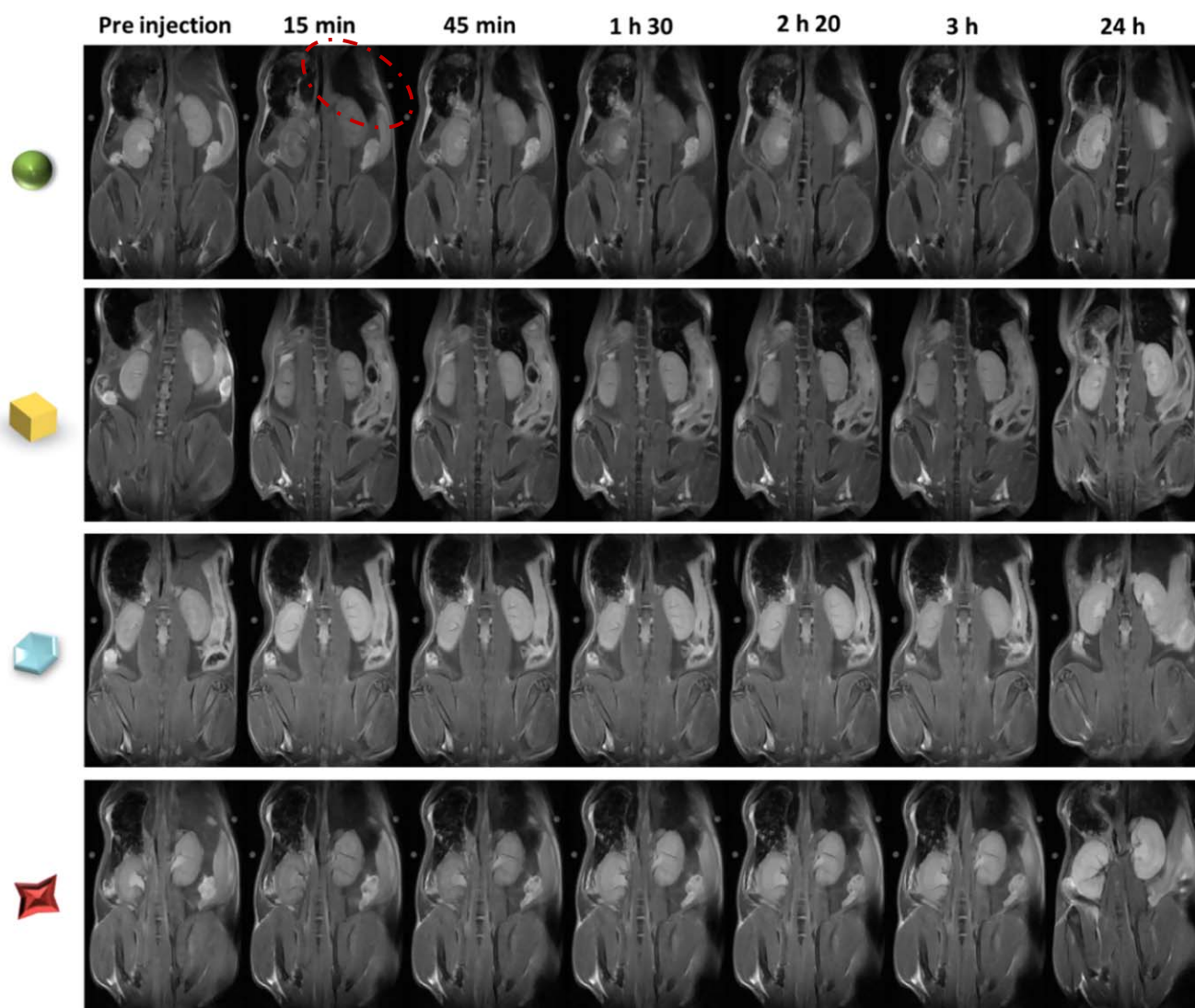


**Figure 10.**  $T_2$  weighted images acquired with a spin echo sequence ( $TR = 2000$  ms,  $TE = 17$  ms, coronal orientation), red circle for liver.

non-homogeneous magnetic field of the magnet leading to a large heterogeneity of the transfection. The slight increase in cell mortality (apoptosis and necrosis) compared to the control is in agreement with a poor internalization of our dendronized NPs as it has been observed with 10 nm spheres [24]. Magnetofection allowed increasing the observed levels of cell death by apoptosis and it is related to a larger cell internalization as it has been demonstrated above (section 3.3.2). It is important to notice that NPI presented equivalent result to those shapes whereas the MH measurements in solution were weak. This might be due to the viscosity of the cell and the large surface of the NPI. Large necrotic cell death percentage was observed after magnetofection. It is interesting to notice that compared to the SAR values measured at magnetic field amplitude and frequency close to those used for the *in vitro* studies (395 kHz,  $12 \text{ kA m}^{-2}$ ), NPI, that presented no macroscopic heat (heat of the NP suspension) increase, induced cell death. Such a result could be explained by the formation of hot spot locally

high enough to induce cell death but not a macroscopic heating [70].

This preliminary study showed the potential of the anisotropic shaped nano-objects towards MH treatment. Also, the poor results observed for the NC indicated that such NC can be ruled out for further studies.

#### 4. Conclusion

Iron oxide NPs presenting various anisotropic shapes were tested for their use both in MRI and MH. We demonstrated that the four dendronized shaped NPs present a good colloidal stability in physiological media, although an aggregation of nanocubes was observed due to their more difficult dendronization. The obtained  $T_2$  MRI CA properties were promising with  $r_2$  values larger than those of the commercial product and standard dendronized 10 nm spheres. In addition, high  $T_2$  values are reached even under a low magnetic field (0.41 T), indicating that they can be used in various MRI

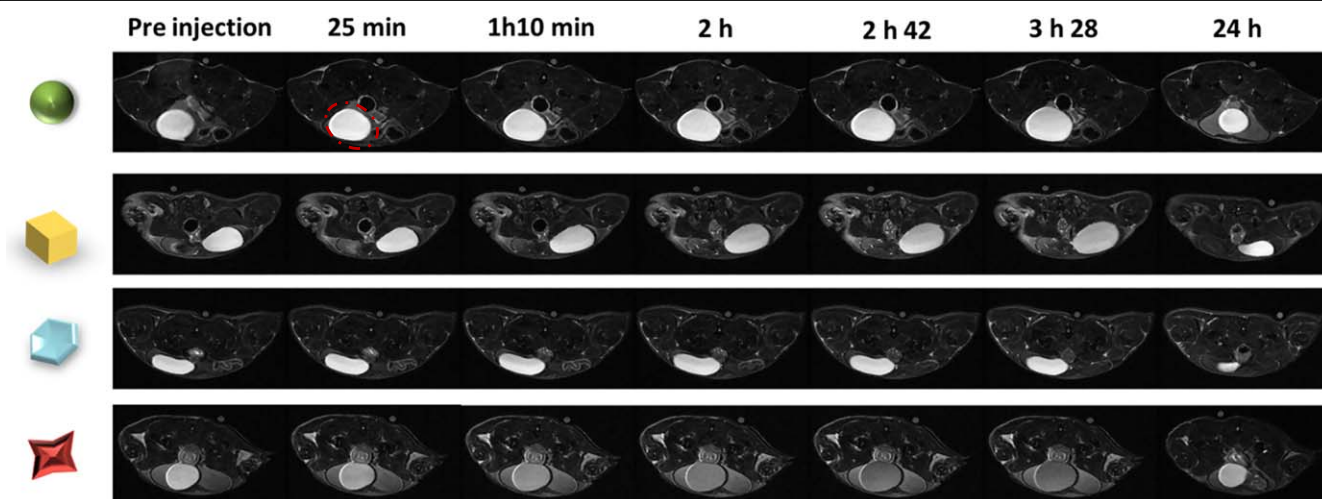


**Figure 11.**  $T_2$  weighted images acquired with a spin echo sequence ( $TR = 7726$  ms,  $TE = 52$  ms, axial orientation), the red circle the bladder.

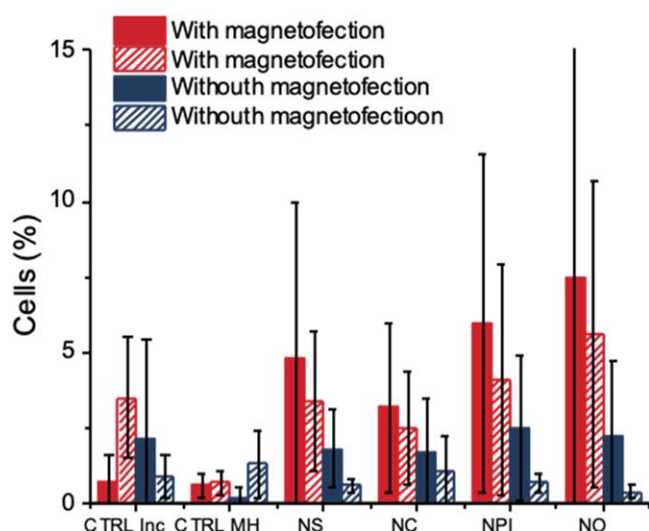


**Figure 12.** Percentage of Apoptotic (plain) and Necrotic (stripped) cells. Red with magnetofection and blue without magnetofection.

apparatus with the same efficiency. Plates did present an interesting behaviour with a slight  $T_1$  effect detected on ghost images at low concentration due to the large iron rich surfaces they present. Though this effect disappears when the concentration increases and  $T_2$  effect becomes the strongest. SAR values measured for all shapes showed that shape anisotropy increased the observed heat dissipation of the NPs, as seen in the case of NO compared to NS.

Cell studies showed that while providing a good colloidal stability, the dendron coating prevents NPs from non-specific internalisation. Magnetofection can help to internalize the NPs as measured with ICP-AES and flow cytometry.

*In vivo* biodistribution evaluated by MRI showed the suitability of dendronized shaped NPs as *in vivo* CA for MRI. A strong contrast constant with time was noticed even with low NPs amounts in organs. Urinary and hepato-biliary elimination pathways were observed though some NPs accumulated in the

liver. Longer analyses times will be necessary to observe eventually a decrease of the NPs signal in the liver, as previously observed for dendronized 10 nm sized NPs.

Magnetic hyperthermia performed on cells with internalized NPs showed limited effect on cell viability due to low NP internalisation. Magnetofection allowed to increase locally the amount of internalized NPs. This effect was used to generate a first proof of concept for the studies of shape control for optimized properties.

Further work is needed using a targeting ligand to improve cell internalization to measure precisely the variation in efficiency between shapes.

## Acknowledgments

The Region Alsace, France, and the Labex Chimie des Systemes Complexes, University of Strasbourg, France are gratefully acknowledged for the doctoral fellowship to Geoffrey Cotin. This research project was also co-funded by Labex CSC, Alsace contre le cancer, INCA (project PRTK14, THERAMAG 2014-225) and the INTERREG project NANOTRANSMED. The authors thank COST Action RADIOMAG (TD1402), supported by COST (European Cooperation in Science and Technology), Morgane Rabineau for epifluorescence imaging and Nadia Messaddeq for cells TEM imaging. The authors thank the Centre for Microscopy and Molecular Imaging (CMMI, supported by the European Regional Development Fund and the Walloon Region). This work was supported by the Fond National de la Recherche Scientifique (FNRS), UIAP VII, ARC Programmes of the French Community of Belgium and the Walloon region (Gadolymp and Holocancer programmes).

## Conflicts of interest

There are no conflicts to declare.

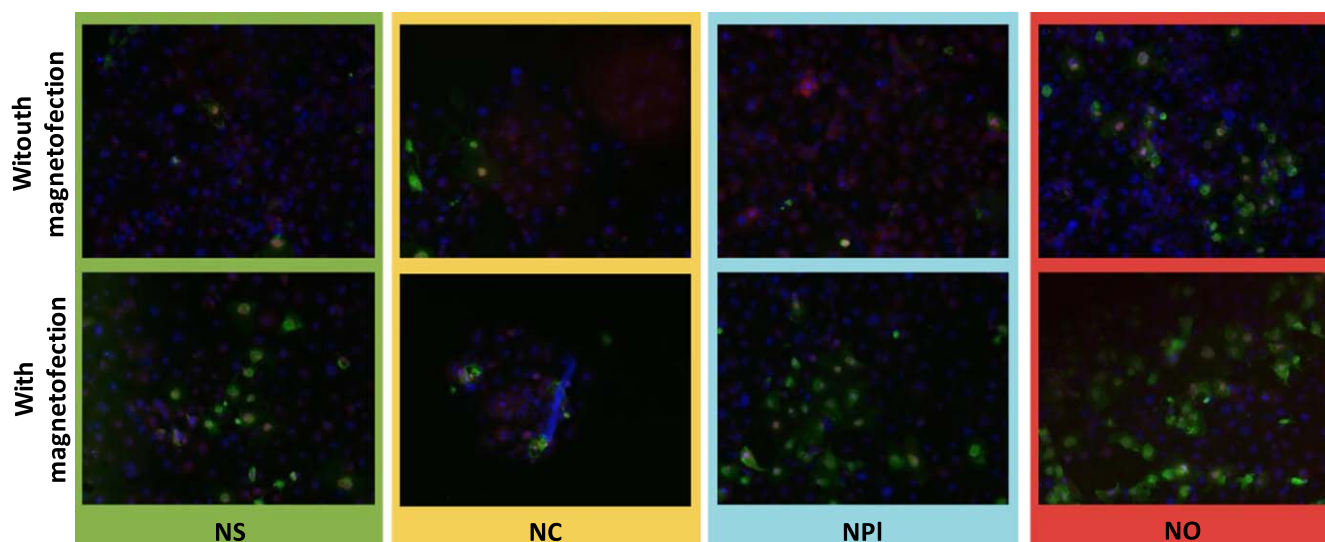


Figure 13. Epifluorescence images of cells after MH treatment, nuclei in blue, apoptotic cells in green and necrotic cells in red.

## ORCID iDs

A Boos <https://orcid.org/0000-0002-9918-3884>  
 D Mertz <https://orcid.org/0000-0002-6745-8978>  
 S Laurent <https://orcid.org/0000-0002-2589-3250>  
 F Meyer <https://orcid.org/0000-0002-5275-3421>  
 S Begin-Colin <https://orcid.org/0000-0002-2293-2226>

## References

- [1] Liong M, Lu J, Kovochich M, Xia T, Ruehm S G, Nel A E, Tamanoi F and Zink J I 2008 Multifunctional inorganic nanoparticles for imaging, targeting, and drug delivery *ACS Nano* **2** 889–96
- [2] Kim J, Piao Y and Hyeon T 2009 Multifunctional nanostructured materials for multimodal imaging, and simultaneous imaging and therapy *Chem. Soc. Rev.* **38** 372–90
- [3] De M, Ghosh P S and Rotello V M 2008 Applications of nanoparticles in biology *Adv. Mater.* **20** 4225–41
- [4] Mornet S, Vasseur S, Grasset F and Duguet E 2004 Magnetic nanoparticle design for medical diagnosis and therapy *J. Mater. Chem.* **14** 2161–75
- [5] Fang C and Zhang M 2009 Multifunctional magnetic nanoparticles for medical imaging applications *J. Mater. Chem.* **19** 6258–66
- [6] Pankhurst Q A, Connolly J, Jones S K and Dobson J 2003 Applications of magnetic nanoparticles in biomedicine *J. Phys. D: Appl. Phys.* **36** R167
- [7] Mura S and Couvreur P 2012 Nanotheranostics for personalized medicine *Adv. Drug Deliv. Rev.* **64** 1394–416
- [8] Choi K Y, Liu G, Lee S and Chen X 2012 Theranostic nanoplateforms for simultaneous cancer imaging and therapy: current approaches and future perspectives *Nanoscale* **4** 330–42
- [9] Mertz D, Sandre O and Bégin-Colin S 2017 Drug releasing nanoplateforms activated by alternating magnetic fields *Biochim. Biophys. Acta-Gen. Subjects* **1861** 1617–41
- [10] Blanco-Andujar C, Walter A, Cotin G, Bordeianu C, Mertz D, Felder-Flesch D and Begin-Colin S 2016 Design of iron oxide-based nanoparticles for MRI and magnetic hyperthermia *Nanomedicine* **11** 1889–910
- [11] Thanh N T 2012 *Magnetic Nanoparticles: From Fabrication to Clinical Applications* (Boca Raton, FL: CRC Press)
- [12] Cotin G, Piant S, Mertz D, Felder-Flesch D and Begin-Colin S 2017 *Iron Oxide Nanoparticles for Biomedical Application: Synthesis, Functionalization and Application* (Amsterdam: Elsevier)
- [13] Stiriba S-E, Frey H and Haag R 2002 Dendritic polymers in biomedical applications: from potential to clinical use in diagnostics and therapy *Angew. Chem., Int. Ed. Engl.* **41** 1329–34
- [14] Duncan R and Izzo L 2005 Dendrimer biocompatibility and toxicity *Adv. Drug Deliv. Rev.* **57** 2215–37
- [15] Cloninger M J 2002 Biological applications of dendrimers *Curr. Opin. Chem. Biol.* **6** 742–8
- [16] Rolland O, Turrin C-O, Caminade A-M and Majoral J-P 2009 Dendrimers and nanomedicine: multivalency in action *New J. Chem.* **33** 1809–24
- [17] Walter A et al 2015 Validation of a dendron concept to tune colloidal stability, MRI relaxivity and bioelimination of functional nanoparticles *J. Mater. Chem. B* **3** 1484–94
- [18] Walter A, Garofalo A, Bonazza P, Meyer F, Martinez H, Fleutot S, Billotey C, Taleb J, Felder-Flesch D and Begin-Colin S 2017 Effect of the functionalization process on the colloidal, magnetic resonance imaging, and bioelimination properties of mono- or bisphosphonate-anchored dendronized iron oxide nanoparticles *Chem. Plus. Chem.* **82** 647–59
- [19] Walter A, Garofalo A, Parat A, Martinez H, Felder-Flesch D and Bégin-Colin S 2015 Functionalization strategies and dendronization of iron oxide nanoparticles *Nanotechnol. Rev.* **4** 581
- [20] Ghobril C, Popa G, Parat A, Billotey C, Taleb J, Bonazza P, Begin-Colin S and Felder-Flesch D 2013 A bisphosphonate tweezers and clickable PEGylated PAMAM dendrons for the preparation of functional iron oxide nanoparticles displaying renal and hepatobiliary elimination *Chem. Commun.* **49** 9158–60
- [21] Basly B et al 2013 Effect of the nanoparticle synthesis method on dendronized iron oxides as MRI contrast agents *Dalton Trans.* **42** 2146–57
- [22] Lamanna G et al 2011 Dendronized iron oxide nanoparticles for multimodal imaging *Biomaterials* **32** 8562–73



- [23] Basly B, Felder-Flesch D, Perriat P, Billotey C, Taleb J, Pourroy G and Begin-Colin S 2010 Dendronized iron oxide nanoparticles as contrast agents for MRI *Chem. Commun.* **46** 985–7
- [24] Bordeianu C, Parat A, Affolter-Zbaraszczuk C, Muller R N, Boutry S, Begin-Colin S, Meyer F, Laurent S and Felder-Flesch D 2017 How a grafting anchor tailors the cellular uptake and *in vivo* fate of dendronized iron oxide nanoparticles *J. Mater. Chem. B* **5** 5152–64
- [25] Maier-Hauff K *et al* 2007 Intracranial thermotherapy using magnetic nanoparticles combined with external beam radiotherapy: results of a feasibility study on patients with glioblastoma multiforme *J. Neuro-Oncol.* **81** 53–60
- [26] Maier-Hauff K, Ulrich F, Nestler D, Niehoff H, Wust P, Thiesen B, Orawa H, Budach V and Jordan A 2011 Efficacy and safety of intratumoral thermotherapy using magnetic iron-oxide nanoparticles combined with external beam radiotherapy on patients with recurrent glioblastoma multiforme *J. Neuro-Oncol.* **103** 317–24
- [27] MagForce 2019 The Nanomedicine Company <http://magforce.de/en/home.html>
- [28] Dennis C L and Ivkov R 2013 Physics of heat generation using magnetic nanoparticles for hyperthermia *Int. J. Hyperth.* **29** 715–29
- [29] Thiesen B and Jordan A 2008 Clinical applications of magnetic nanoparticles for hyperthermia *Int. J. Hyperth.* **24** 467–74
- [30] Deatsch A E and Evans B A 2014 Heating efficiency in magnetic nanoparticle hyperthermia *J. Magn. Magn. Mater.* **354** 163–72
- [31] Kolosnjaj-Tabi J *et al* 2014 Heat-generating iron oxide nanocubes: subtle ‘destructurators’ of the tumoral microenvironment *ACS Nano* **8** 4268–83
- [32] Hergt R, Dutz S, Müller R and Zeisberger M 2006 Magnetic particle hyperthermia: nanoparticle magnetism and materials development for cancer therapy *J. Phys.: Condens. Matter.* **18** S2919
- [33] Gazeau F, Lévy M and Wilhelm C 2008 Optimizing magnetic nanoparticle design for nanothermotherapy *Nanomedicine* **3** 831–44
- [34] Walter A *et al* 2014 Mastering the shape and composition of dendronized iron oxide nanoparticles to tailor magnetic resonance imaging and hyperthermia *Chem. Mater.* **26** 5252–64
- [35] Habib A H, Ondeck C L, Chaudhary P, Bockstaller M R and McHenry M E 2008 Evaluation of iron-cobalt/ferrite core-shell nanoparticles for cancer thermotherapy *J. Appl. Phys.* **103** 07A307
- [36] Smolensky E D, Park H-Y E, Zhou Y, Rolla G A, Marjańska M, Botta M and Pierre V C 2013 Scaling laws at the nanosize: the effect of particle size and shape on the magnetism and relaxivity of iron oxide nanoparticle contrast agents *J. Mater. Chem. B* **1** 2818
- [37] Joshi H M, Lin Y P, Aslam M, Prasad P V, Schultz-Sikma E A, Edelman R, Meade T and Dravid V P 2009 Effects of shape and size of cobalt ferrite nanostructures on their MRI contrast and thermal activation *J. Phys. Chem. C* **113** 17761–7
- [38] de Montferrand C, Hu L, Milosevic I, Russier V, Bonnin D, Motte L, Brioude A and Lalatonne Y 2013 Iron oxide nanoparticles with sizes, shapes and compositions resulting in different magnetization signatures as potential labels for multiparametric detection *Acta Biomater.* **9** 6150–7
- [39] Guardia P, Di Corato R, Lartigue L, Wilhelm C, Espinosa A, Garcia-Hernandez M, Gazeau F, Manna L and Pellegrino T 2012 Water-soluble iron oxide nanocubes with high values of specific absorption rate for cancer cell hyperthermia treatment *ACS Nano* **6** 3080–91
- [40] Kostopoulou A, Velu S K P, Thangavel K, Orsini F, Brintakis K, Psycharakis S, Ranella A, Bordonali L, Lappas A and Lascialfari A 2014 Colloidal assemblies of oriented maghemite nanocrystals and their NMR relaxometric properties *Dalton Trans.* **43** 8395–404
- [41] Das R, Alonso J, Nemati Porshokouh Z, Kalappattil V, Torres D, Phan M-H, Garaio E, García J A, Sanchez Llamazares J L and Srikanth H 2016 Tunable high aspect ratio iron oxide nanorods for enhanced hyperthermia *J. Phys. Chem. C* **120** 10086–93
- [42] Milosevic I, Jouni H, David C, Warmont F, Bonnin D and Motte L 2011 Facile microwave process in water for the fabrication of magnetic nanorods *J. Phys. Chem. C* **115** 18999–9004
- [43] Rosensweig R E 2002 Heating magnetic fluid with alternating magnetic field *J. Magn. Magn. Mater.* **252** 370–4
- [44] Hergt R and Dutz S 2007 Magnetic particle hyperthermia—biophysical limitations of a visionary tumour therapy *J. Magn. Magn. Mater.* **311** 187–92
- [45] Murugan K, Choonara Y E, Kumar P, Bijukumar D, du Toit L C and Pillay V 2015 Parameters and characteristics governing cellular internalization and trans-barrier trafficking of nanostructures *Int. J. Nanomed.* **10** 2191–206
- [46] Chen L, Xiao S, Zhu H, Wang L and Liang H 2016 Shape-dependent internalization kinetics of nanoparticles by membranes *Soft Matter* **12** 2632–41
- [47] Cotin G *et al* 2018 Unravelling the thermal decomposition parameters for the synthesis of anisotropic iron oxide nanoparticles *Nanomaterials* **8** 881
- [48] Pichon B P *et al* 2011 Microstructural and magnetic investigations of wüstite-spinel core-shell cubic-shaped nanoparticles *Chem. Mater.* **23** 2886–900
- [49] Baaziz W, Pichon B P, Fleutot S, Liu Y, Lefevre C, Grenèche J-M, Toumi M, Mhiri T and Begin-Colin S 2014 Magnetic iron oxide nanoparticles: reproducible tuning of the size and nanosized-dependent composition, defects, and spin canting *J. Phys. Chem. C* **118** 3795–810
- [50] Chevallier P, Walter A, Garofalo A, Veksler I, Lagueux J, Bégin-Colin S, Felder-Flesch D and Fortin M-A 2014 Tailored biological retention and efficient clearance of pegylated ultra-small MnO nanoparticles as positive MRI contrast agents for molecular imaging *J. Mater. Chem. B* **2** 1779
- [51] Cotin G *et al* 2018 Evaluating the critical roles of precursor nature and water content when tailoring magnetic nanoparticles for specific applications *ACS Appl. Nano Mater.* **1** 4306–16
- [52] Walter A *et al* 2015 Modulation of relaxivity, suspension stability, and biodistribution of dendronized iron oxide nanoparticles as a function of the organic shell design *Part. Part. Syst. Charact.* **32** 552–60
- [53] Daou T J, Begin-Colin S, Grenèche J M, Thomas F, Derory A, Bernhardt P, Legaré P and Pourroy G 2007 Phosphate adsorption properties of magnetite-based nanoparticles *Chem. Mater.* **19** 4494–505
- [54] Marins J A, Montagnon T, Ezzaier H, Hurel C, Sandre O, Baltrunas D, Mazeika K, Petrov A and Kuzhir P 2018 Colloidal stability of aqueous suspensions of polymer-coated iron oxide nanorods: implications for biomedical applications *ACS Appl. Nano Mater.* **1** 6760–72
- [55] Vuong Q L, Berret J-F, Fresnais J, Gossuin Y and Sandre O 2012 A universal scaling law to predict the efficiency of magnetic nanoparticles as MRI  $T_2$ -contrast agents *Adv. Healthcare Mater.* **1** 502–12
- [56] Yoon T-J, Lee H, Shao H and Weissleder R 2011 Highly magnetic core-shell nanoparticles with unique magnetization mechanism *Angew. Chem., Int. Ed. Engl.* **50** 4663–6
- [57] Laurent S, Bridot J-L, Elst L V and Muller R N 2010 Magnetic iron oxide nanoparticles for biomedical applications *Future Med. Chem.* **2** 427–49

- [58] Gossuin Y, Gillis P, Hocq A, Vuong Q L and Roch A 2009 Magnetic resonance relaxation properties of superparamagnetic particles *Wiley Interdiscip. Rev. Nanomed. Nanobiotechnol.* **1** 299–310
- [59] Zhou Z, Zhao Z, Zhang H, Wang Z, Chen X, Wang R, Chen Z and Gao J 2014 Interplay between longitudinal and transverse contrasts in  $\text{Fe}_3\text{O}_4$  nanoplates with (111) exposed surfaces *ACS Nano* **8** 7976–85
- [60] Zhao Z et al 2013 Octapod iron oxide nanoparticles as high-performance  $T_2$  contrast agents for magnetic resonance imaging *Nat. Commun.* **4** 2266
- [61] Pösel E, Kloust H, Tromsdorf U, Janschel M, Hahn C, Maßlo C and Weller H 2012 Relaxivity optimization of a PEGylated iron-oxide-based negative magnetic resonance contrast agent for  $T_2$ -weighted spin-echo imaging *ACS Nano* **6** 1619–24
- [62] Berret J-F, Schonbeck N, Gazeau F, El Kharrat D, Sandre O, Vacher A and Airiau M 2006 Controlled clustering of superparamagnetic nanoparticles using block copolymers: design of new contrast agents for magnetic resonance imaging *J. Am. Chem. Soc.* **128** 1755–61
- [63] Ai H, Flask C, Weinberg B, Shuai X-T, Pagel M D, Farrell D, Duerk J and Gao J 2005 Magnetite-loaded polymeric micelles as ultrasensitive magnetic-resonance probes *Adv. Mater.* **17** 1949–52
- [64] Mehdaoui B, Tan R P, Meffre A, Carrey J, Lachaize S, Chaudret B and Respaud M 2013 Increase of magnetic hyperthermia efficiency due to dipolar interactions in low anisotropy magnetic nanoparticles: theoretical and experimental results *Phys. Rev. B* **87** 174419
- [65] Serantes D, Simeonidis K, Angelakeris M, Chubykalo-Fesenko O, Marciello M, Morales M, del P, Baldomir D and Martinez-Boubeta C 2014 Multiplying magnetic hyperthermia response by nanoparticle assembling *J. Phys. Chem. C* **118** 5927–34
- [66] Billotey C, Wilhelm C, Devaud M, Bacri J C, Bittoun J and Gazeau F 2003 Cell internalization of anionic maghemite nanoparticles: quantitative effect on magnetic resonance imaging *Magn. Reson. Med.* **49** 646–54
- [67] Patil R M, Thorat N D, Shete P B, Bedge P A, Gavde S, Joshi M G, Tofail S A M and Bohara R A 2018 Comprehensive cytotoxicity studies of superparamagnetic iron oxide nanoparticles *Biochem. Biophys. Rep.* **13** 63–72
- [68] Hemery G, Genevois C, Couillaud F, Lacomme S, Gontier E, Ibarboure E, Lecommandoux S, Garanger E and Sandre O 2017 Monocore versus multicore magnetic iron oxide nanoparticles: uptake by glioblastoma cells and efficiency for magnetic hyperthermia *Mol. Syst. Des. Eng.* **2** 629–39
- [69] Blanco-Andujar C, Ortega D, Southern P, Nesbitt S A, Thanh N T K and Pankhurst Q A 2015 Real-time tracking of delayed-onset cellular apoptosis induced by intracellular magnetic hyperthermia *Nanomedicine* **11** 121–36
- [70] Guisasola E, Baeza A, Asín L, Fuente J M D L and Vallet-Regí M 2018 Heating at the nanoscale through drug-delivery devices: fabrication and synergic effects in cancer treatment with nanoparticles *Small Methods* **2** 1800007